Engineering Fracture Mechanics 312 (2024) 110625

Contents lists available at ScienceDirect

Engineering Fracture Mechanics

journal homepage: www.elsevier.com/locate/engfracmech

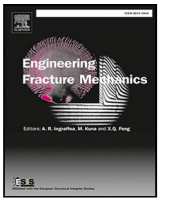

Multiaxial failure of dual-phase elastomeric composites

Mohit Goswami [a,*], Piyush Gupta [b], Yoav Lev [a], Santanu Chattopadhyay [b], Konstantin Volokh [a]

[a] Faculty of Civil and Environmental Engineering, Technion - Israel Institute of Technology, Haifa, 3200003, Israel
[b] Rubber Technology Centre, Indian Institute of Technology Kharagpur, India

ARTICLE INFO

Keywords:
Bulge test
Constitutive modeling
Finite element analysis (FEA)
Cavitation analysis

ABSTRACT

The natural rubber (NR) and styrene butadiene rubber (SBR) based composites are used in several industrial applications, mainly tires. The mechanical properties can be tailored by blending them in appropriate ratios. In the present study, blended polymer–matrix composites are tested for uniaxial and bulge tests. Simultaneous constitutive modeling with failure description is done for uniaxial and equibiaxial test results. Using the computational modeling we study the problem of cavitation and compare these results with morphological analysis. The finite element analysis (FEA) is used to analyze state of stress throughout the bulge. We find that the rubber composites can behave contradictorily under different types of mechanical testing environments. For instance, the pressure at failure for SBR composite is found to be 3% more than NR composite under bulge test. However, tensile strength of NR composite is found to 40% more than that of SBR composite, when tested uniaxially. The critical hydrostatic tension corresponding to onset of cavitation is observed to decreasing by more than 20% when NR composite is compared with SBR composite. The dual phase rubber composite with 25% NR and 75% SBR exhibits better mechanical properties, when compared with other blended composites.

1. Introduction

The elastomeric composites are used in various industrial and daily life products, mainly in tires. Tires are constructed using rubbers, steel cords, and fabrics. However, durability and strength majorly depend on type of rubber composite used. Natural rubber (NR) based composites are used for their unique property called strain induced crystallization (SIC) which enhances their mechanical strength [1–3]. The styrene butadiene rubber (SBR) composites excel in terms of high abrasion resistance, flex resistance, and crack initiation resistance [4,5]. The fatigue life of NR is better than SBR at large strains; the reverse is true for small strains [6]. The blending of both rubbers can result in composites with favorable mechanical properties; however, it is important to optimize the blend ratio.

Hess et al. blended NR and SBR in 50:50 ratio to elaborate mechanical properties by varying type of carbon black (CB) [7]. The rubber composites filled with high abrasion furnace (HAF) CB were found to exhibit better mechanical properties. CB is also found to be having high reinforcing efficacy and better fracture properties when compared with silica [8,9]. Latter is the reason for choosing HAF CB as filler in our study. It is also evident that NR/SBR blends filled with CB outperform in terms of mechanical properties after thermal ageing [10]. The type of curing system and the structural properties of the chain influence cross-linking and chain degradation [11]. The conventional curing system is used in the present study, which ensures higher number of poly-sulfidic and di-sulfidic crosslinks, resulting in improved mechanical properties.

* Corresponding author.
E-mail addresses: mohit@technion.ac.il (M. Goswami), cvolokh@technion.ac.il (K. Volokh).

https://doi.org/10.1016/j.engfracmech.2024.110625
Received 3 August 2024; Received in revised form 8 October 2024; Accepted 5 November 2024

Table 1
Compounding formulation of rubber composites.

Material	Ingredients, phr					Fuction
	N_{100}	$N_{75}S_{25}$	$N_{50}S_{50}$	$N_{25}S_{75}$	S_{100}	
NR	100	75	50	25	0	Raw elastomer
SBR	0	25	50	75	100	Raw elastomer
CB(N330)	45	45	45	45	45	Filler
Peptizer	0.2	0.2	0.2	0.2	0.2	Catalyst
ZnO	5	5	5	5	5	Activator
Stearic acid	2	2	2	2	2	Activator
TQ	1	1	1	1	1	Antioxidant
6PPD	1.5	1.5	1.5	1.5	1.5	Antiozonant
Processing oil	5	5	5	5	5	Plasticizer
CBS	1	1	1	1	1	Accelerator
TMTD	0.2	0.2	0.2	0.2	0.2	Accelerator
PVI	0.15	0.15	0.15	0.15	0.15	Scorch inhibitor
Sulfur	2.5	2.5	2.5	2.5	2.5	Curing agent

The rubber composites used in engineering applications experience multiaxial state of stress. Latter is the reason to perform bulge test, where equibiaxial stress is observed at the top of the pole [12]. In this procedure, a thin sheet of rubber composite is clamped at the edges and pressure is supplied to inflate the material. In the bulge test, the stress–strain state is not uniform and the maximum equibiaxial stresses and strains develop on the top of the inflated membrane, where the damage also starts. Localization of damage on the top of the membrane provides robust testing processes unaffected by the boundary conditions. However, the interpretation of results is not trivial due to non-uniformity in strain distribution. Balakhovsky et al. elaborated a finite element method based procedure to interpret bulge test results [13]. Meunier et al. investigated behavior of silicone rubbers undergoing bulge tests [14]. Savio et al. proposed a new theoretical model to interpret bulge test results, but this model is confined to very low strains and lacks a description of failure [15]. These bulge tests are not limited to only inflation by means of air, they can be done by using various gases, even water [16]. The literature lacks bulge tests of blended rubber composites. However, there are several studies on crack propagation and fracture of rubber composites using experimental and finite element methods [17–20]. The micro-cracks are initiated by cavity formation by filler-matrix debonding depending on the interfacial bonding, which depends on several factors like curing temperature, crosslinking, and type of filler. The latter phenomenon is generally expressed in constitutive models by using energy limiters.

Still, the literature lacks information on the formation of cracks, which depends on the instigation of cavities and their propagation through the rubber matrix [21–23]. The study of these phenomena becomes very difficult and costly using experimental investigations. In-situ scanning electron microscopy (SEM) assisted mechanical testing devices can be used to see void nucleation [24–26]. Eric et al. studied cavitation using in-Situ synchrotron X-ray microtomography, and following this methodology, several researchers investigated different types of rubber composites [27,28]. The other simple way is to use theoretical models developed concerning instability during cavitation [29]. There are several constitutive models for various classes of polymers [30], but they lack a description of failure. Latter is needed to study cavitation theoretically. These theoretical studies are confined to single-phase rubber composites, and the need arises to extend them to dual-phase rubber composites.

In summary, we envisage developing NR/SBR blended rubber composites filled with CB and optimizing the ratio of rubbers in the elastomer matrix. The biaxial testing is done using in house developed bulge test device. The material modeling is done with failure description using simultaneous fit methodology. Morphological analysis is performed to study the phase separation and dispersion of filler in the composites. The cavitation instability in developed rubber composites is studied thoroughly.

2. Materials and methods

The following materials were used to prepare the rubber composites: Natural rubber (Ribbed Smoked Sheet) RSS-3, Emulsion Styrene-Butadiene rubber (SBR) 1502, High Abrasion Furnace Carbon Black (N330), Zinc oxide (ZnO), Stearic acid, N-Cyclohexyl-2-benzothiazole Sulfenamide (CBS), Tetramethylthiuram Disulfide (TMTD), 2,2,4-trimethyl 1,2-dihydroquinoline (TQ), N-(1,3-Dimethylbutyl)-N′-phenyl-p-phenylenediamine (6PPD), N-(Cyclohexylthio) phthalimide (PVI), Peptizer, Processing oil, and Sulfur. The raw rubbers were procured from Arlanxeo Performance Elastomers Germany, CB was purchased from PCBL India, and other chemicals were purchased from local vendors.

The ingredients mentioned above are mixed conventionally to ensure high cure efficiency as per methodology described in Fig. 1. The quantities of ingredients are shown in Table 1. The optimum cure temperature (T_{C90}) for each compound was evaluated using Monsanto R100 oscillating disc rheometer (ODR) by performing rheological studies at 150 °C. The rheographs of rubber composites are shown in Fig. 2, and cure characteristics are exhibited in Table 2. Later, these compounds were vulcanized using a hydraulic compression machine (David Bridge and Group) at a temperature of 150 °C, maintaining a pressure of 5 MPa till T_{C90} obtained from rheological studies, to produce rubber composite sheets (2 mm thick).

Atomic force microscopy (AFM) is performed to study phase morphology and filler dispersion in rubber composites using Park system NX10 AFM in non-contact mode. The specimens for microscopy were prepared from the cryo- fractured surface of composites, which were cleaned using a solvent to get rid of contaminants. The resonance frequency is set to be 330 kHz at a tip radius of 10 nm.

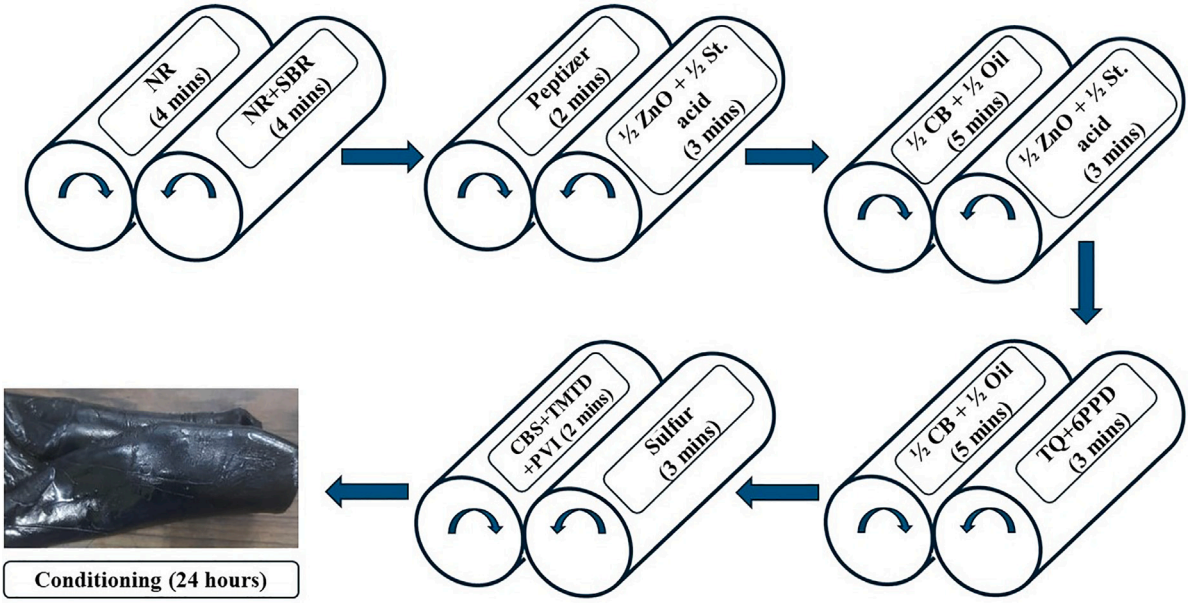

Fig. 1. Methodology of compounding.

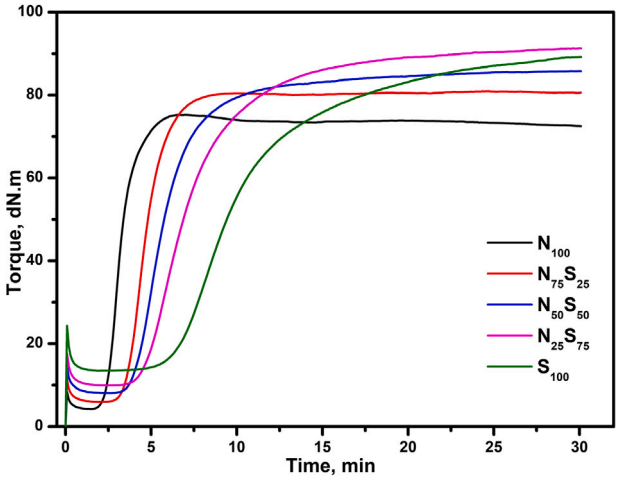

Fig. 2. Rheographs of rubber composites.

Table 2
Cure characteristics of rubber composites.

Rubber composite	T_{S2}, min	T_{C90}, min	ΔT, dN m	CRI, min^{-1}
N_{100}	2.15	4.51	71.02	42.39
$N_{75}S_{25}$	3.23	6.34	75.01	32.23
$N_{50}S_{50}$	3.70	9.32	77.77	17.79
$N_{25}S_{75}$	4.23	12.80	81.3	11.67
S_{100}	5.72	18.64	75.75	7.74

The dumbbell-shaped smooth samples were made from vulcanized rubber composite sheets with a gauge length of 33 mm and a cross-section of 6 mm × 2 mm (ASTM D412, type C). These specimens were uniaxially tested using Zwick-Roell UTM at room temperature and an extension rate of 500 mm/min. Three samples of each rubber composite are tested to ensure repeatability, and average of these results are considered for further analysis.

The bulge test [31,32] is used to interpret equibiaxial response of rubber composites. The readers are referred to our previous works [12,33] to understand the bulge test procedure. The schematic view and experimental setup of the in house-developed bulge

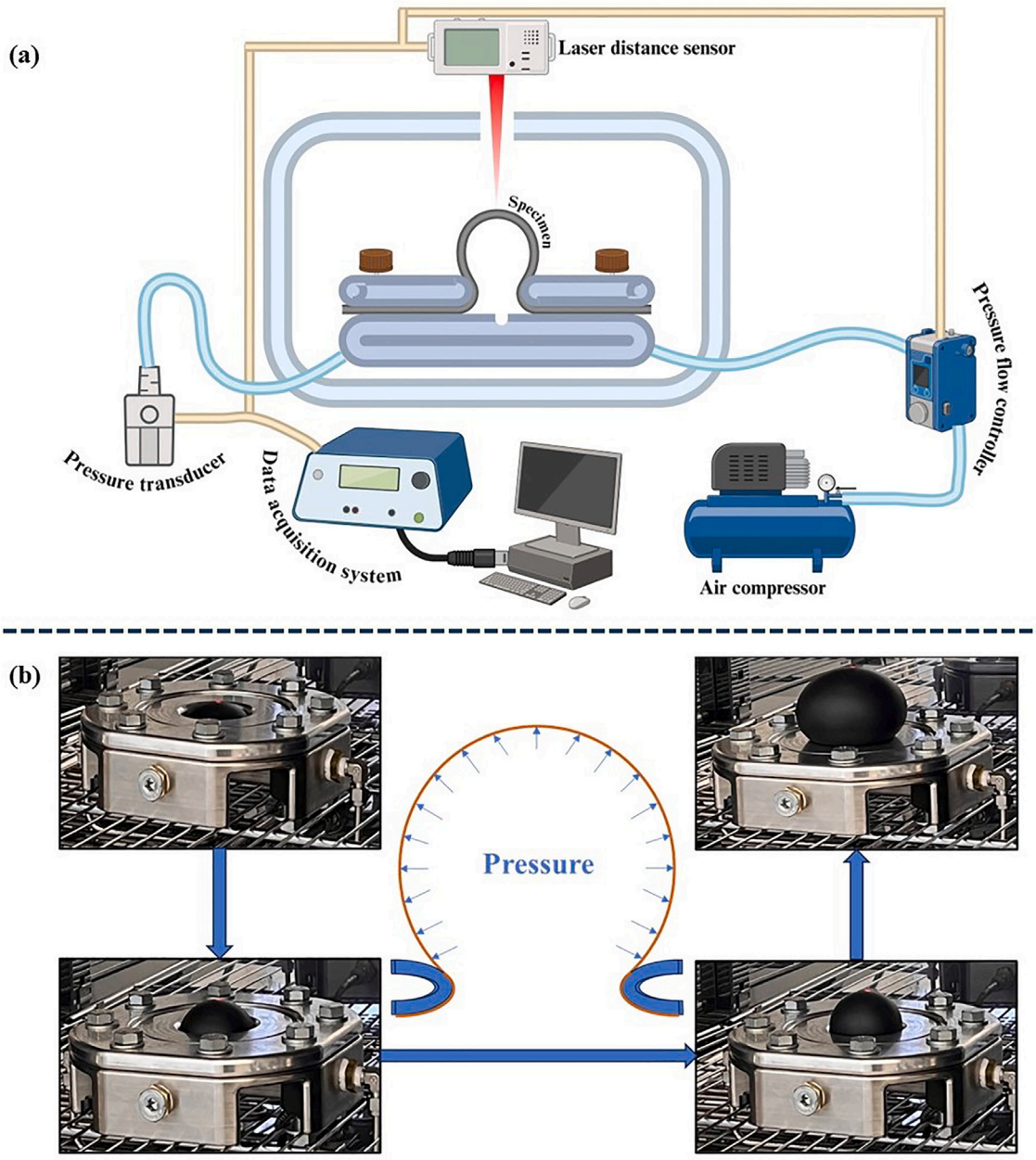

Fig. 3. (a) Experimental setup and (b) process for bulge test.

test device are elaborated in Fig. 3. The rubber composites (15 cm × 15 cm) are clamped between top and bottom flanges of bulge test device. The top flange (15 mm thick) has a circular opening 60 mm diameter. Channel 'A' is used to supply compressed air through the bottom flange. The pressure is supplied very slowly (0.02 bar/s) to avoid viscous effects. Channel 'B' is attached with a pressure transducer (range 0–10 bar, 0.5% accuracy) to record pressure inside bulge test device. The laser distance sensor is used to record vertical displacement (δ) at the top of bulge. All the measurements are recorded using NI data acquisition card and stored using in house developed LabView program.

3. Theory

In this section we discuss about constitutive modeling of rubber composites (including description for failure). The calibration of these models with experimental results obtained using uniaxial and biaxial experiments is also discussed. We encourage readers to go through [34,35] for a general background.

3.1. The free Helmholtz energy with failure

The Helmholtz free energy per unit reference volume can be written as

$$w(\mathbf{F},\gamma) = w_f - \mathcal{H}(\gamma) w_e(\mathbf{F}), \tag{1}$$

where

$$w_e(\mathbf{F}) = \frac{\phi}{m}\Gamma\left[\frac{1}{m}, \left(\frac{W(\mathbf{F})}{\phi}\right)^m\right], \qquad w_f = w_e(\mathbf{1}), \tag{2}$$

and $\Gamma(s,x) = \int_x^\infty t^{s-1}e^{-t}dt$ is the upper incomplete gamma function; $\mathbf{F}$ is the deformation gradient; $w_f(\mathbf{F})$ and $w_e(\mathbf{F})$ corresponds to failure energy and elastic energy, respectively; $W(\mathbf{F})$ is the strain energy function of intact material; m is a dimensionless parameter, which controls sharpness of transition to material failure; ϕ is the energy limiter; $\mathbf{1}$ is second order identity tensor; $\mathcal{H}(\gamma)$ is the Heaviside step function, which prevents material healing: $\mathcal{H}(\gamma) = 0$ if $\gamma = 0$ and $\mathcal{H}(\gamma) = 1$, otherwise. The switch parameter $\gamma \in (-\infty, 0]$ is calculated using the evolution equation

$$\dot{\gamma} = -\mathcal{H}\left(\zeta - \frac{w_e}{w_f}\right), \qquad \gamma(0) = 0, \tag{3}$$

where $0 < \zeta \ll 1$ is the precision limit. We assume, the rubber composites used in this study to be nearly incompressible ($\det\mathbf{F} = 1$), as they have carbon black as filler. We use the thermodynamic reasoning elaborated in [36] and calculate the first Piola–Kirchhoff stress tensor ($\mathbf{P}$) as

$$\mathbf{P} = \frac{\partial w}{\partial \mathbf{F}} - \Pi\mathbf{F}^{-\mathrm{T}} = -\mathcal{H}(\gamma)\frac{\partial w_e}{\partial \mathbf{F}} - \Pi\mathbf{F}^{-\mathrm{T}} = \mathcal{H}(\gamma)\exp\left[-\left(\frac{W(\mathbf{F})}{\phi}\right)^m\right]\frac{\partial W}{\partial \mathbf{F}} - \Pi\mathbf{F}^{-\mathrm{T}}, \tag{4}$$

where Π is the Lagrange multiplier, which can be determined using boundary/equilibrium conditions. Alternatively, we can write Cauchy stress as

$$\boldsymbol{\sigma} = \mathbf{P}\mathbf{F}^{\mathrm{T}} = \mathcal{H}(\gamma)\exp\left[-\left(\frac{W(\mathbf{F})}{\phi}\right)^m\right]\frac{\partial W}{\partial \mathbf{F}}\mathbf{F}^{\mathrm{T}} - \Pi\mathbf{1}. \tag{5}$$

3.2. Strain energy function and experimental calibration

We can write deformation gradient as

$$\mathbf{F} = \lambda_1\mathbf{e}_1 \otimes \mathbf{e}_1 + \lambda_2\mathbf{e}_2 \otimes \mathbf{e}_2 + \lambda_3\mathbf{e}_3 \otimes \mathbf{e}_3, \tag{6}$$

where $\mathbf{e}_1$, $\mathbf{e}_2$, $\mathbf{e}_3$ are Cartesian basis vectors and λ_1, λ_2, λ_3 are their corresponding principal stretches. We consider three term Ogden hyperelastic model [37,38] as strain energy function, which can be written as

$$W = \sum_{j=1}^{3}\frac{\mu_j}{\alpha_j}({\lambda_1}^{\alpha_j} + {\lambda_2}^{\alpha_j} + {\lambda_3}^{\alpha_j} - 3), \qquad \mu_j\alpha_j > 0 \tag{7}$$

where μ_j and α_j are material parameters. Using Eq. (4), we can write diagonal principal values of the first Piola–Kirchhoff stress tensor as

$$P_1 = \frac{\partial w}{\partial \lambda_1} - \frac{\Pi}{\lambda_1}, \qquad P_2 = \frac{\partial w}{\partial \lambda_2} - \frac{\Pi}{\lambda_2}, \qquad P_3 = \frac{\partial w}{\partial \lambda_3} - \frac{\Pi}{\lambda_3}. \tag{8}$$

For uniaxial deformation we have

$$\lambda_1 = \lambda, \qquad \lambda_2 = \lambda_3 = \sqrt{\frac{1}{\lambda}}, \tag{9}$$

and, consequently using Eqs. (7) and (8), we can write diagonal principal values of the Piola–Kirchhoff stresses as

$$P_1 = \exp\left(-\frac{W^m}{\phi^m}\right)\left(\mu_1\lambda^{\alpha_1-1} + \mu_2\lambda^{\alpha_2-1} + \mu_3\lambda^{\alpha_3-1}\right) - \frac{\Pi}{\lambda}, \tag{10}$$

and

$$P_2 = P_3 = \exp\left(-\frac{W^m}{\phi^m}\right)\left(\mu_1(\sqrt{\lambda})^{1-\alpha_1} + \mu_2(\sqrt{\lambda})^{1-\alpha_2} + \mu_3(\sqrt{\lambda})^{1-\alpha_3}\right) - \Pi\sqrt{\lambda}. \tag{11}$$

Since there is no unloading in this mode, we have eliminated the step function. There are no lateral stresses in uniaxial tension, thus equating Eq. (11) to zero, we evaluate the Lagrange multiplier as

$$\Pi = \exp\left(-\frac{W^m}{\phi^m}\right)\left(\mu_1(\sqrt{\lambda})^{-\alpha_1} + \mu_2(\sqrt{\lambda})^{-\alpha_2} + \mu_3(\sqrt{\lambda})^{-\alpha_3}\right), \tag{12}$$

substituting the above result in Eq. (10), we obtain

$$P_u = P_1 = \exp\left(-\frac{W^m}{\phi^m}\right)\left(\mu_1(\lambda^{\alpha_1} - \lambda^{-0.5\alpha_1}) + \mu_2(\lambda^{\alpha_2} - \lambda^{-0.5\alpha_2}) + \mu_3(\lambda^{\alpha_3} - \lambda^{-0.5\alpha_3})\right)\left(\frac{1}{\lambda}\right), \tag{13}$$

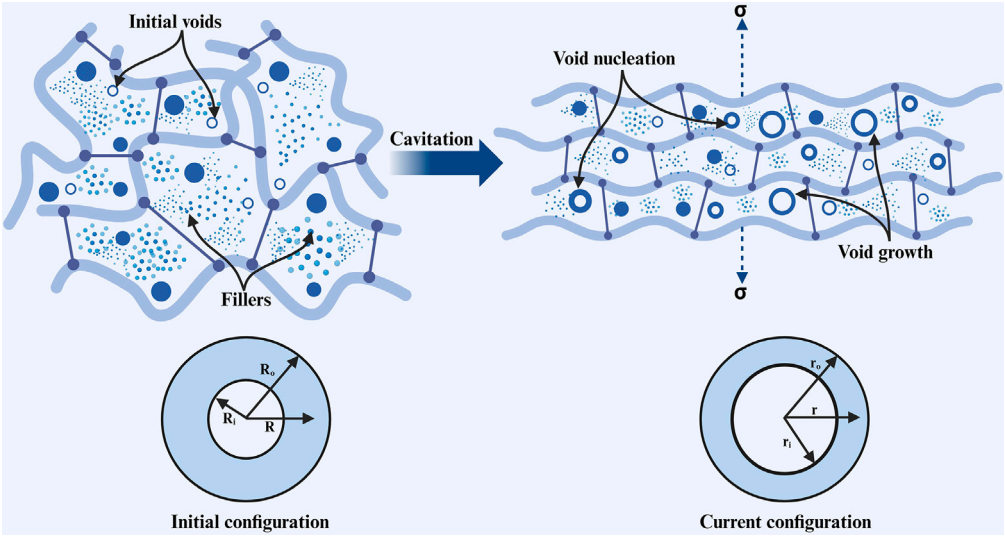

Fig. 4. Expansion of void in a spherical material particle.

or we can write constitutive equations for Cauchy stress using (5) as

$$\sigma_u = \exp\left(-\frac{W^m}{\phi^m}\right)\left(\mu_1(\lambda^{\alpha_1} - \lambda^{-0.5\alpha_1}) + \mu_2(\lambda^{\alpha_2} - \lambda^{-0.5\alpha_2}) + \mu_3(\lambda^{\alpha_3} - \lambda^{-0.5\alpha_3})\right). \tag{14}$$

The principal stretches for equibiaxial tension take the form

$$\lambda_1 = \lambda_2 = \lambda, \qquad \lambda_3 = \frac{1}{\lambda^2}, \tag{15}$$

using above procedure for uniaxial tension and assuming $P_3 = 0$ we calculate Lagrange multiplier for equibiaxial tension as

$$\Pi = \exp\left(-\frac{W^m}{\phi^m}\right)\left(\mu_1(\lambda)^{-2\alpha_1} + \mu_2(\lambda)^{-2\alpha_2} + \mu_3(\lambda)^{-2\alpha_3}\right), \tag{16}$$

we can evaluate stresses for equibiaxial tension as

$$P_{bi} = \exp\left(-\frac{W^m}{\phi^m}\right)\left(\mu_1(\lambda^{\alpha_1} - \lambda^{-2\alpha_1}) + \mu_2(\lambda^{\alpha_2} - \lambda^{-2\alpha_2}) + \mu_3(\lambda^{\alpha_3} - \lambda^{-2\alpha_3})\right)\left(\frac{1}{\lambda}\right), \tag{17}$$

and

$$\sigma_{bi} = \exp\left(-\frac{W^m}{\phi^m}\right)\left(\mu_1(\lambda^{\alpha_1} - \lambda^{-2\alpha_1}) + \mu_2(\lambda^{\alpha_2} - \lambda^{-2\alpha_2}) + \mu_3(\lambda^{\alpha_3} - \lambda^{-2\alpha_3})\right). \tag{18}$$

The experimental results obtained using uniaxial tests can be fit using constitutive equation elaborated in Eq. (13). The material parameters are calculated using nonlinear least squares optimization method with the curve fitting toolbox of MATLAB [39]. However, the calibration for biaxial test is not trivial. The finite element simulations are used to calibrate material parameters of constitutive model for bulge tests. The top aluminium flange is modeled as a rigid, rigid surface. However, discretization of rubber composites is done using three noded axisymmetric elements. The interaction property between rubber and aluminium is governed by keeping 0.3 as coefficient of friction. The pressure is applied as load on inner surface of axisymmetric beam elements. 8401 four-node bilinear, reduced integration with hourglass control, hybrid elements are used for analysis; mesh convergence analysis is performed prior simulation to optimize number of elements. The finite element analysis (FEA) is performed using ABAQUS [40]. The pressure and vertical displacement at top (δ) obtained form FEA is compared with respect to experimental results for each iteration with different sets of material parameters. The optimization of material parameters is done using optimization toolbox of [39]. The optimized material parameters are thereafter used to interpret material response under equibiaxial tension using Eq. (18).

3.3. Cavitation

The unstable expansion of voids caused by hydrostatic stresses in a elastomeric composite is known as cavitation. Gent et al. discovered the yielding of micron-scale cavities into the apparent ones when they conducted "poker-chip" experiments on natural rubber specimens [41]. However, this phenomenon has not been studied for NR/SBR blended rubber composites. Volokh postulated instabilities in single-phase rubber composites due to cavitation [29]; however, in the present work, we extend it for blended rubber composites. We assume that deformation is centrally symmetric and write law of deformation as

$$r = r(R), \qquad \theta = \Theta, \qquad \omega = \Omega, \tag{19}$$

where spherical coordinates R, Θ, Ω corresponds to initial configuration whereas r, θ, ω represent current configuration as shown in Fig. 4. The principal stretches in this instance coincide with the stretches along the spherical coordinate lines, and the deformation gradient is diagonal. Using the latter condition, we write principal stretches as

$$\lambda_1 = \frac{\partial r}{\partial R}, \qquad \lambda_2 = \lambda_3 = \frac{r}{R}, \tag{20}$$

where subscript 1 corresponds to radial direction, whereas subscripts 2 and 3 represent hoop directions. Since we consider rubber composites used in this study to be incompressible and during deformation, their volume is conserved ($R^3 - {R_i}^3 = r^3 - {r_i}^3$). The diagonal components of Cauchy stress can be written as

$$\sigma_1 = \sigma_{rr} = \lambda_1 \frac{\partial w}{\partial \lambda_1} - \Pi, \tag{21}$$

$$\sigma_2 = \sigma_{\theta\theta} = \lambda_2 \frac{\partial w}{\partial \lambda_2} - \Pi, \tag{22}$$

$$\sigma_3 = \sigma_{\omega\omega} = \lambda_3 \frac{\partial w}{\partial \lambda_3} - \Pi. \tag{23}$$

We write boundary conditions as

$$\sigma_1(r_i) = 0, \qquad \sigma_1(r_o) = g, \tag{24}$$

and equilibrium condition as

$$2\frac{\sigma_1 - \sigma_2}{r} + \frac{\partial \sigma_1}{\partial r} = 0, \tag{25}$$

which can be integrated as

$$\sigma_1(r_o) - \sigma_1(r_i) = g = 2\int_{r_i}^{r_o} \frac{\sigma_2 - \sigma_1}{r} dr = 2\int_{r_i}^{r_o} \left(\lambda_2 \frac{\partial w}{\partial \lambda_2} - \lambda_1 \frac{\partial w}{\partial \lambda_1}\right) \frac{dr}{r} \tag{26}$$

where g is hydrostatic tension. The incompressibility condition states

$$\lambda_1 \lambda_2 \lambda_3 = \frac{\partial r}{\partial R} \frac{r^2}{R^2} = 1, \tag{27}$$

and considering volume conservation during deformation, we have

$$R = (r^3 - {r_i}^3 + {R_i}^3)^{1/3}. \tag{28}$$

We make this formulation dimensionless in terms of length and rewrite Eq. (26) as

$$g = 2\int_{\bar{r_i}}^{\bar{r_o}} \left(\lambda_2 \frac{\partial w}{\partial \lambda_2} - \lambda_1 \frac{\partial w}{\partial \lambda_1}\right) \frac{d\bar{r}}{\bar{r}}, \tag{29}$$

where

$$\bar{r} = \frac{r}{R_i}, \qquad \bar{R} = \frac{R}{R_i}, \qquad \bar{r_i} = \frac{r_i}{R_i}, \qquad \bar{r_o} = \frac{r_o}{R_i}, \tag{30}$$

and

$$\lambda_1 = \frac{R^2}{r^2} = \frac{\bar{R}^2}{\bar{r}^2}, \qquad \lambda_2 = \lambda_3 = \frac{r}{R} = \frac{\bar{r}}{\bar{R}}. \tag{31}$$

4. Results and discussions

The scorch time (T_{S2}) and optimum cure time (T_{C90}) increases with the increasing quantity of SBR in the blend; this behavior can be attributed to the un-saturation of NR in the composites. The cure rate index (CRI) decreases with increasing SBR; this is due to increment in styrene content, which provides more cross-linking sites and lowers the CRI. The difference between highest and lowest values of torque in a rheo-curve is known as ΔT which reflects rigidity of a rubber composite [42]. It is observed that blended rubber composites have higher ΔT when compared with single-phase rubber composites. This is attributed to presence of styrene and high cross-linking efficacy in blended rubber composites.

The morphological analysis utilizing AFM is shown in Fig. 5. The $N_{50}S_{50}$ composite exhibits a co-continuous morphology with some carbon black aggregates, while $N_{25}S_{75}$ shows the coexistence structure of globule and percolation for NR domains in the SBR matrix, owing to the higher viscosity of the NR phase. Hence, the domain size of the irregular globule in $N_{25}S_{75}$ is also larger than that of the irregularly shaped structure in $N_{75}S_{25}$. We followed the standard mixing procedure where NR and SBR are mixed first, and thereafter, CB is added. Furthermore, SBR has a higher affinity towards CB, resulting in a highly filled SBR phase, and interphase in $N_{50}S_{50}$, whereas the NR phase is lowly filled. This trend can also be observed in S_{100}, which results in aggregates of higher size when compared with N_{100}.

The tensile strength was seen to be decreasing with increasing SBR content in rubber composites, however, the ultimate tensile strain was more in case of blended rubber composites. The comparison between experimental and FEA results concerning pressure and vertical displacement (δ) is shown in Fig. 6. The maximum pressure at failure decreases till we increase SBR content up to 50%,

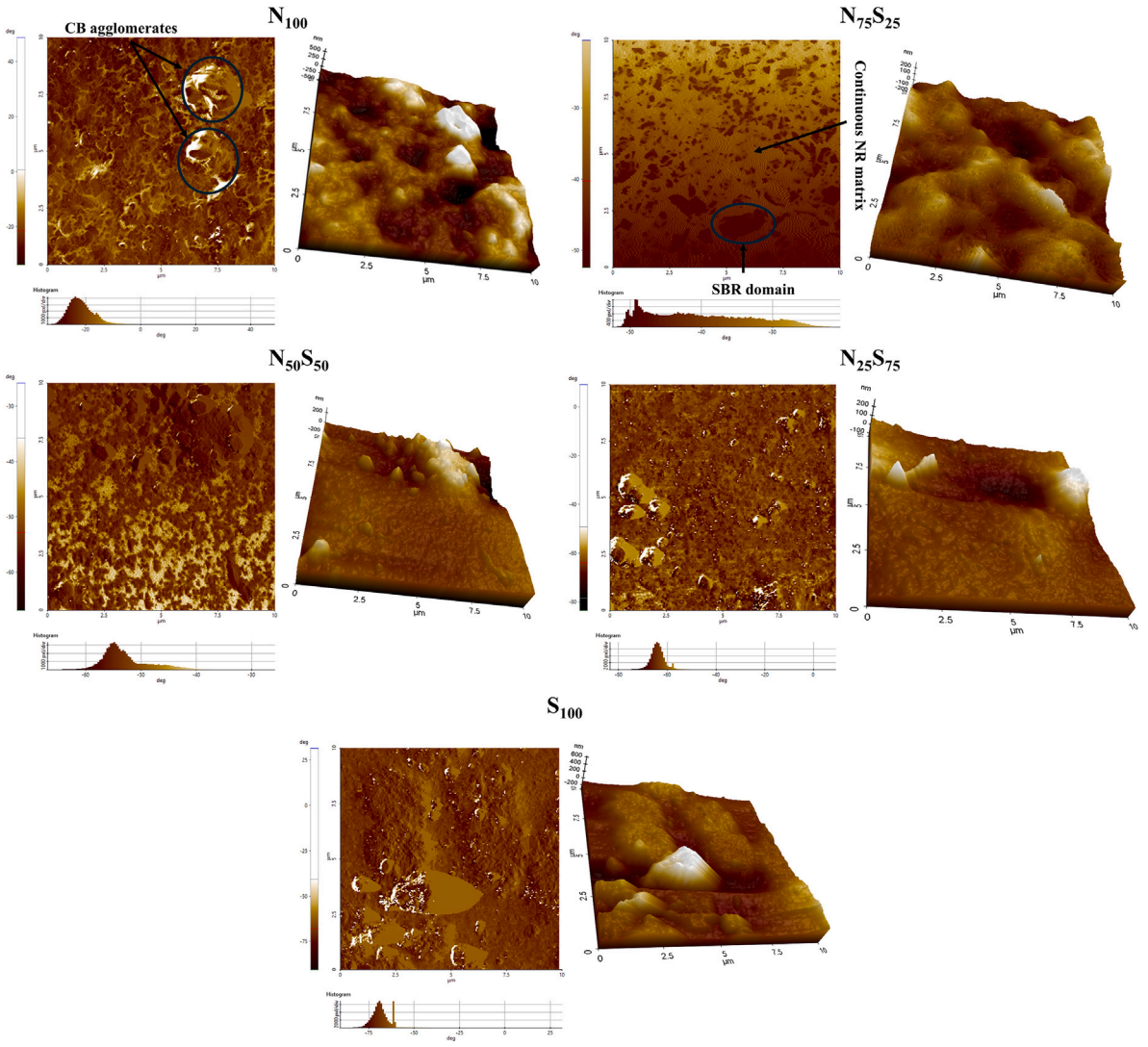

Fig. 5. AFM micrographs of rubber composites.

whereas, it increases when SBR content is more than 50% in rubber composites. The latter observation can be related to increased styrene content, which enhances the rigidity, favoring the distribution of biaxial stresses.

The failed specimen of rubber composites for bulge tests can be seen in Fig. 7(a). It is observed that blown area increases with increasing SBR content in rubber composites and is maximum for single phase SBR composite. The reason for the latter observation is an increment of styrene content in the rubber composites having a high content of SBR. The FEA results (Fig. 7(b)) revealed that the ratio of maximum axial to lateral stress is higher for composites having more NR content, which can be associated with an increment in rigidity in composites having a high concentration of SBR favoring accommodation of higher lateral stress.

The material parameters obtained for three term Ogden model were used to evaluate experimental equibiaxial tension response of rubber composites. These results are further used for further theoretical modeling. Since we deal with different sets experimental results, the need arises for simultaneous fit using a single material model. Ogden et al. introduced a methodology based on optimizing material parameters and relative errors [43]. The squared residuals for both uniaxial and equibiaxial test fits are calculated and minimized. The material parameters obtained from simultaneous modeling are shown in Table 3 and the comparison with experimental results can be visualized in Fig. 8.

The cross-link density of a rubber composite reveals about density of connections between polymeric chains. The latter property of rubber composites is directly proportional to initial shear modulus (G), which is calculated as

$$G = \frac{1}{2}\sum_{j=1}^{3}\mu_j\alpha_j. \tag{32}$$

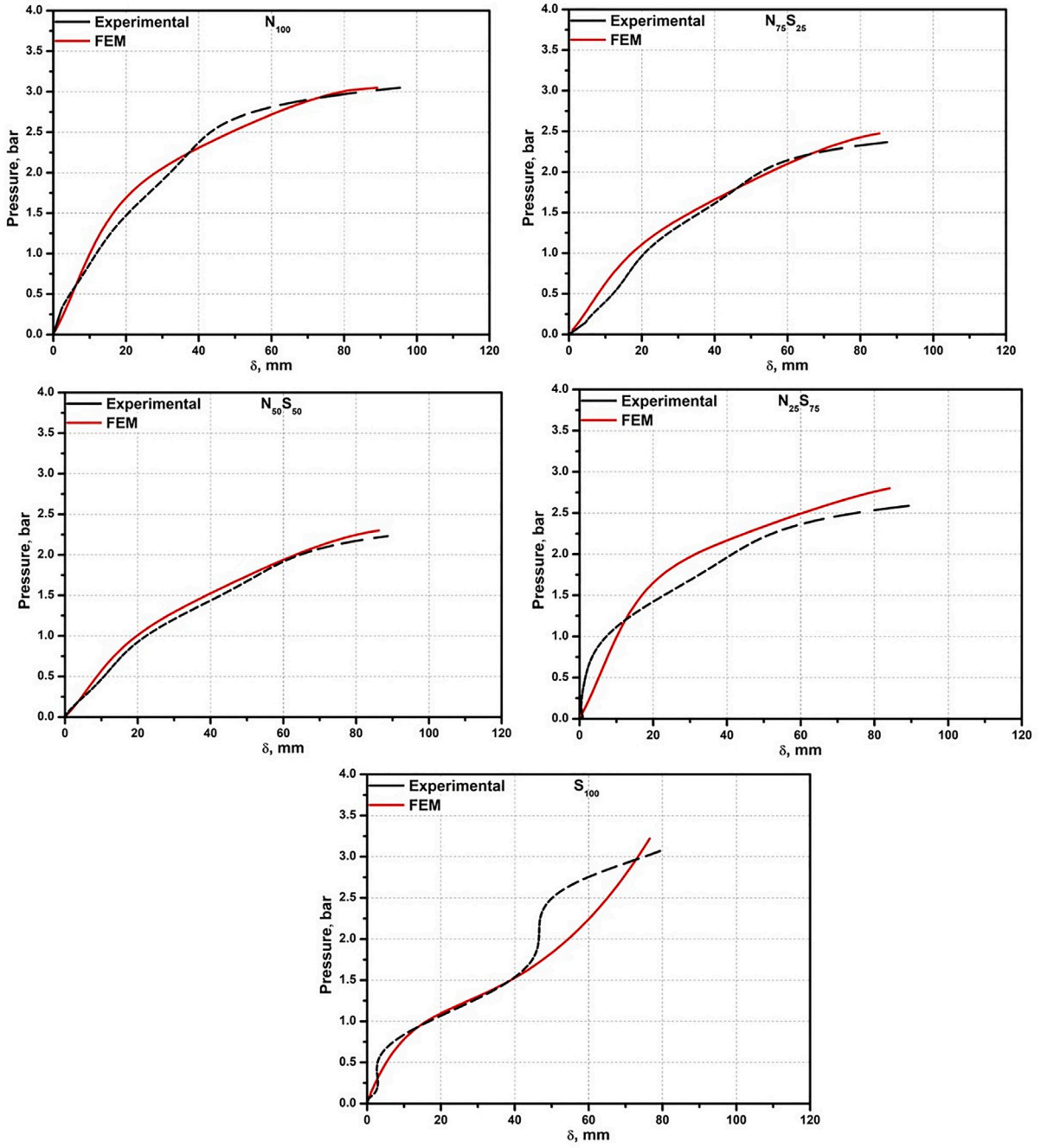

Fig. 6. Experimental and simulation results for pressure-vertical displacement response of rubber composites during bulge test.

Table 3
Material parameters for Ogden model with three parameters with energy limiter (m=50).

Rubber composite	μ_1, MPa	μ_2, MPa	μ_3, MPa	α_1	α_2	α_3	ϕ, MPa
N_{100}	−0.400	−0.058	0.547	−1.495	−1.495	2.865	80
$N_{75}S_{25}$	−0.131	−0.214	0.331	−1.569	−1.569	2.934	72
$N_{50}S_{50}$	−9.999	−0.133	0.413	−0.001	−1.844	2.810	58
$N_{25}S_{75}$	−10	−0.220	0.497	−0.022	−1.727	2.724	55
S_{100}	−10	−0.030	0.482	−0.043	−2.844	2.696	45

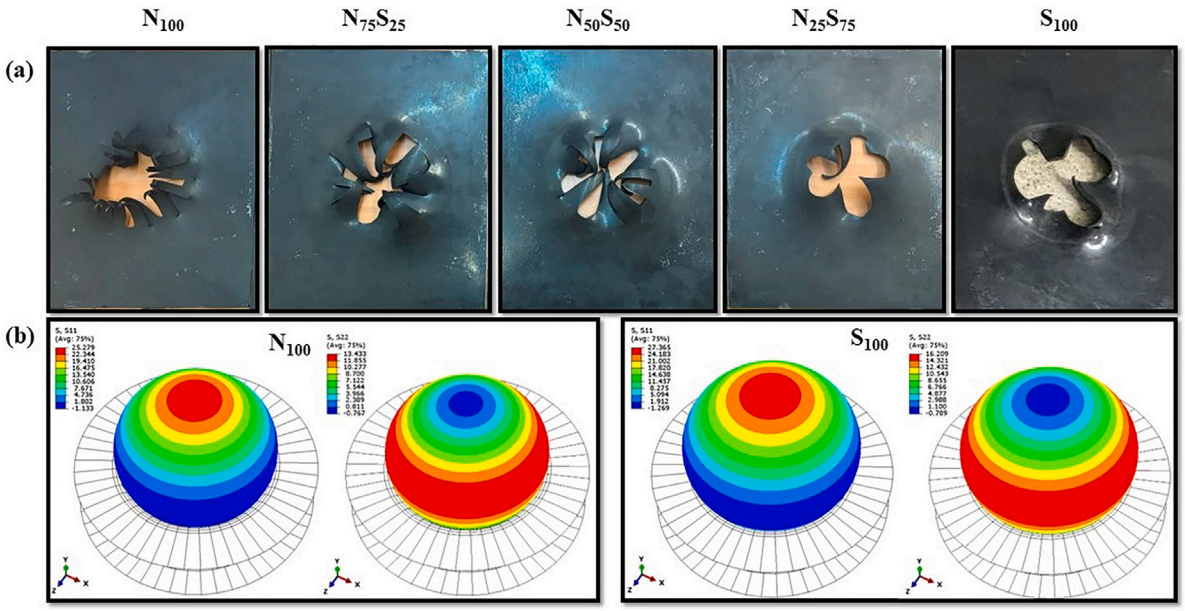

Fig. 7. (a) Rubber composites after failure, and (b) distribution of axial and lateral stress in single phase rubber composites.

Table 4
Material parameters for energy limiter function.

Control rubber in composite	β_1, MPa	β_2, MPa	β_3, MPa	β_4, MPa	ϕ_0, MPa
NR	−373.3	752	−456.7	113	45
SBR	−373.3	741.3	−440.7	37.66	80

G decreases by 19.3% when we compare N_{100} with S_{100}. Whereas, for blended rubber composites, $N_{25}S_{75}$ is found to have maximum value of G. The latter observations can be associated with crosslink density of rubber composites.

The material parameter 'm' governs the sharpness of transition to the material failure on the stress–strain response. There is no reported literature concerning value of m for blended rubber composites; however, based on optimization we assume $m = 50$. The energy limiter (ϕ) decreases with increasing SBR content in rubber composites. ϕ drops by 43.75% when we compare single phase NR composite (N_{100}) with SBR composite (S_{100}), which can be attributed to strain induced crystallization in NR. This change is marginal when NR content is reduced from 50% to 25%. The rubber content in these blends is generally optimized as per the required properties; however, the correct interpretation of energy limiter can give a purview of their mechanical properties. It is observed that the energy limiters vary with varying volume fraction (γ) of rubber in the composite. A constitutive equation relating volume fraction and energy limiter based on a polynomial function of fourth degree is derived as

$$\phi = \beta_1\gamma^4 + \beta_2\gamma^3 + \beta_3\gamma^2 + \beta_3\gamma + \phi_0, \tag{33}$$

where ϕ_0 is energy limiter at $\gamma = 0$; β_1, β_2, β_3, and β_4 are material constants. These material constants for varied volume fraction of NR and SBR in the elastomeric composites are shown in Table 4 and the fit can be seen in Fig. 9.

The horizontal lines in Fig. 10 represent onset of instability in material. This phenomenon can only be observed by infusing failure description in the constitutive model. The critical hoop stretch at which voids grow unstable is minimum for single-phase SBR composite, whereas its variation is marginal for dual-phase rubber composites. The hydrostatic tension corresponding to unstable void growth is maximum for N_{100}, whereas when we compare blended rubber composites g is maximum for $N_{25}S_{75}$. These results highly depend on the extent of agglomerates. The histograms shown in Fig. 5 can be correlated with these observations.

5. Conclusion

The current study presents novel results concerning biaxial testing and modeling of blended rubber composites. Mechanical and morphological characterization is done for NR and SBR blended rubber composites with different ratios in elastomeric matrix. The pressure at failure (P_u) increased by 6% while comparing single phase NR composite with SBR composite. However the vertical displacement at failure (δ_u) is decreased by 18%. The trend of these results is different from what we observed in uniaxial tests. The ultimate stress and stretch decreases by 47% and 12%, respectively when we compare single phase NR composite with SBR composite. The latter observation can be related with strain induced crystallization (SIC), which enhances mechanical properties

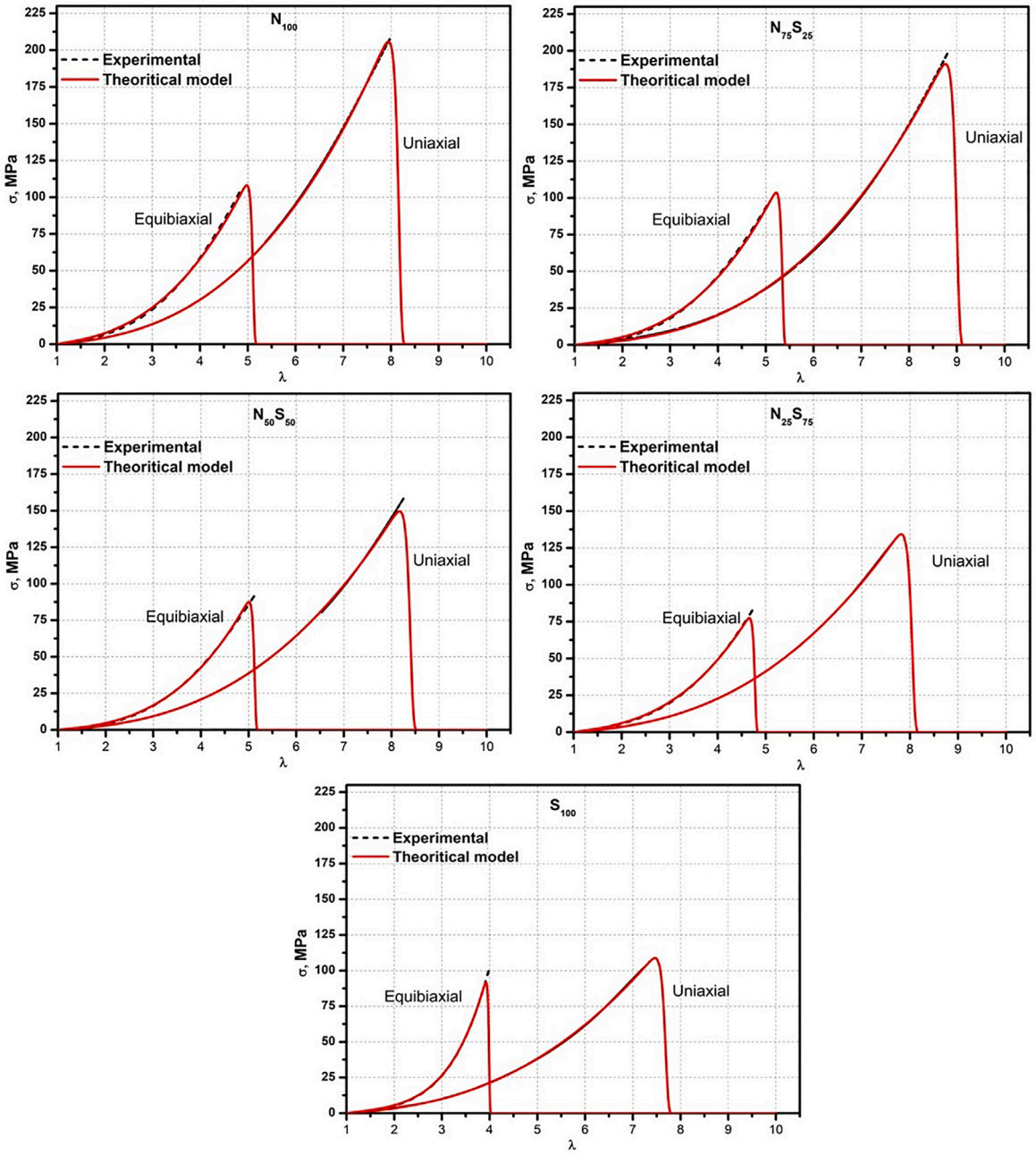

Fig. 8. Comparison between experimental and theoretical model for Cauchy stress versus stretch relationship of rubber composites.

when we perform strain-based experiments (uniaxial tensile test), whereas the SBR performs well in accommodating more stresses due to rigidity provided by styrene. The latter observation motivated us to study biaxial inflation of NR and SBR blended composites.

The interpretation of bulge test is not trivial, and finite element method based optimization is done to calibrate material parameters. These material parameters are thereafter used to interpret equibiaxial results. The Ogden material model with three parameters is used with failure description (energy limiter) for theoretical modeling. These constitutive equations are further used to fit equibiaxial and uniaxial test results of rubber composites, simultaneously. A good correlation is found between fits and experimental results. The energy limiter is decreased by 43.75% when we compare single-phase NR composite with SBR composite. When we increase content of SBR more than 25% in blended composites the change in ϕ is 5%, which can be considered marginal.

The phase separation and extent of agglomeration governs mechanical properties of blended rubber composites. Atomic force microscopy results reveal that the blended composites having 50:50 ratio of NR and SBR exhibit co-continuous morphology with

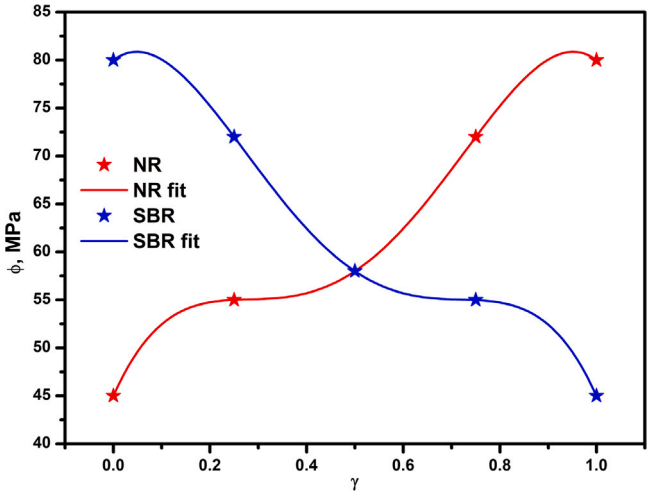

Fig. 9. Energy limiter as a function of volume fraction.

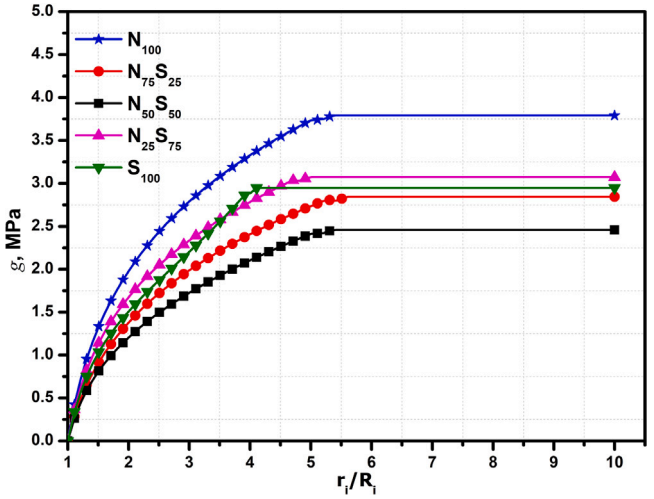

Fig. 10. Hydrostatic tension versus normalized radius for single phase and blended rubber composites.

carbon black aggregates. The blended composite with 75% SBR exhibits coexistence structure of globule and percolation of NR domains in SBR matrix. Similar trend is also observed in cavitation analysis, where critical hydrostatic tension (onset of unstable void growth) increases by 12% when we increase quantity of SBR from 50% to 75% in blended rubber composites. However when we compare single phase NR with SBR critical hydrostatic tension decreases by 23%.

Summarisingly, it can be concluded that NR/SBR blended composite with 25% NR and 75% SBR outperforms most of the mechanical properties. The NR composites are always superior due to strain-induced crystallization, and styrene in SBR composites favors accommodation of biaxial stresses. Furthermore, it will be interesting to see how these composites behave at elevated temperature.

CRediT authorship contribution statement

Mohit Goswami: Writing – original draft, Validation, Software, Methodology, Investigation, Formal analysis, Conceptualization. **Piyush Gupta:** Writing – review & editing, Investigation, Conceptualization. **Yoav Lev:** Writing – review & editing, Software, Methodology, Investigation. **Santanu Chattopadhyay:** Writing – review & editing, Supervision, Conceptualization. **Konstantin Volokh:** Writing – review & editing, Supervision, Project administration, Methodology, Funding acquisition, Conceptualization.

Declaration of competing interest

The authors declare that they have no known competing financial interests or personal relationships that could have appeared to influence the work reported in this paper.

Acknowledgments

The support from the Israeli Ministry of Science and Technology (MOST-0005173) and Israel Science Foundation, Israel (ISF-394/20) is gratefully acknowledged.

Data availability

Data will be made available on request.

References

[1] Gent A, Zhang L-Q. Strain-induced crystallization and strength of rubber. Rubber Chem Technol 2002;75(5):923–34.
[2] Toki S, Fujimaki T, Okuyama M. Strain-induced crystallization of natural rubber as detected real-time by wide-angle X-ray diffraction technique. Polymer 2000;41(14):5423–9.
[3] Tosaka M. Strain-induced crystallization of crosslinked natural rubber as revealed by X-ray diffraction using synchrotron radiation. Polym J 2007;39(12):1207–20.
[4] McCrum NG, Buckley CP, Bucknall CB. Principles of Polymer Engineering. Oxford University Press; 1997.
[5] Berki P, Göbl R, Karger-Kocsis J. Structure and properties of styrene-butadiene rubber (SBR) with pyrolytic and industrial carbon black. Polym Test 2017;61:404–15.
[6] Morton M. Rubber Technology. Springer Science & Business Media; 2013.
[7] Hess W, Chirico V. Elastomer blend properties—Influence of carbon black type and location. Rubber Chem Technol 1977;50(2):301–26.
[8] Goswami M, Ghosh MM, Dalmiya MS, Sharma S, Ghorai SK, Chattopadhyay S. A finite element method based comparative fracture assessment of carbon black and silica filled elastomers: Reinforcing efficacy of carbonaceous fillers in flexible composites. Polym Test 2020;91:106856.
[9] Goswami M, Sharma S, Roychowdhury S, Bordas SP, Chattopadhyay S. Fracture of V-notched natural rubber composites used in heavy-duty tire tread. Eng Fail Anal 2023;150:107358.
[10] Hamed G, Zhao J. Tensile behavior after oxidative aging of gum and black-filled vulcanizates of SBR and NR. Rubber Chem Technol 1999;72(4):721–30.
[11] Jovanović S, Samaržija-Jovanović S, Marković G, Jovanović V, Adamović T, Marinović-Cincović M. Mechanical properties and thermal aging behaviour of polyisoprene/polybutadiene/styrene-butadiene rubber ternary blend reinforced with carbon black. Composites B 2016;98:126–33.
[12] Lev Y, Faye A, Volokh K. Thermoelastic deformation and failure of rubberlike materials. J Mech Phys Solids 2019;122:538–54.
[13] Balakhovsky K, Volokh K. Inflation and rupture of rubber membrane. Int J Fract 2012;177:179–90.
[14] Meunier L, Chagnon G, Favier D, Orgéas L, Vacher P. Mechanical experimental characterisation and numerical modelling of an unfilled silicone rubber. Polym Test 2008;27(6):765–77.
[15] Savio FL, La Rosa G, Bonfanti M. A new theoretical-experimental model deriving from the contactless measurement of the thickness of bulge-tested elastomeric samples. Polym Test 2020;87:106548.
[16] Coccia M, Lattanzi A, Chiappini G, Sasso M, Rossi M. Analysis of the thermomechanical behaviour of SMP in equi-biaxial condition by means of hydraulic bulge test. In: Thermomechanics & infrared imaging, inverse problem methodologies, mechanics of additive & advanced manufactured materials, and advancements in optical methods & digital image correlation, volume 4: Proceedings of the 2021 annual conference on experimental and applied mechanics. Springer; 2022, p. 77–83.
[17] Abu-Qbeitah S, Jabareen M, Volokh KY. Dynamic versus quasi-static analysis of crack propagation in soft materials. J Appl Mech 2022;89(12):121008.
[18] Goswami M, Ghorai SK, Sharma S, Chakraborty G, Chattopadhyay S. Nonlinear fracture assessment and nanomechanical deformation of elastomeric composites: Development of finite element model and experimental validation. Polym Compos 2021;42(7):3572–92.
[19] Abu-Qbeitah S, Jabareen M, Volokh KY. Quasi-static crack propagation in soft materials using the material-sink theory. Int J Mech Sci 2023;248:108160.
[20] Goswami M, Sharma S, Ghosh MM, Kröger NH, Berto F, Chakraborty G, Chattopadhyay S. Finite element method based damage model to characterize effect of geometric configuration on fracture properties of elastomeric composites. Mech Adv Mater Struct 2023;30(11):2149–63.
[21] Le Cam J-B, Huneau B, Verron E, Gornet L. Mechanism of fatigue crack growth in carbon black filled natural rubber. Macromolecules 2004;37(13):5011–7.
[22] Saintier N, Cailletaud G, Piques R. Crack initiation and propagation under multiaxial fatigue in a natural rubber. Int J Fatigue 2006;28(1):61–72.
[23] Mars W, Fatemi A. Nucleation and growth of small fatigue cracks in filled natural rubber under multiaxial loading. J Mater Sci 2006;41:7324–32.
[24] Federico C, Padmanathan H, Koteckỳ O, Rommel R, Rauchs G, Fleming Y, Addiego F. Resolving cavitation in silica-filled styrene-butadiene rubber composites upon cyclic tensile testing. Polym Test 2021;100:107274.
[25] Yakovlev I, Sztucki M, Fleck F, Karimi-Varzaneh HA, Lacayo-Pineda J, Vatterott C, Giese U. Cavity formation in silica-filled rubber compounds observed during deformation by ultra small-angle X-Ray scattering. 2024, arXiv preprint arXiv:2407.08541.
[26] Mashita R, Bito Y, Uesugi K, Hoshino M, Kageyuki I, Kishimoto H, Yashiro W, Kanaya T. Insights into the cavitation morphology of rubber reinforced with a nano-filler. Sci Rep 2023;13(1):5805.
[27] Euchler E, Bernhardt R, Wilde F, Schneider K, Heinrich G, Tada T, Wießner S, Stommel M. First-time investigations on cavitation in rubber parts subjected to constrained tension using in situ synchrotron X-Ray microtomography (SRμCT). Adv Energy Mater 2021;23(11):2001347.
[28] Federico CE, Fleming Y, Koteckỳ O, Rommel R, Philippe A-M, Westermann S, Addiego F. Assessment of strain-induced cavitation of silica-filled styrene-butadiene rubber nanocomposite by synchrotron radiation tomography. Composites B 2022;247:110337.
[29] Volokh K. Cavitation instability in rubber. Int J Appl Mech 2011;3(02):299–311.
[30] Gong Y, Liu F, Zou R, Ye X, Ning H, Hu N, Huang X, Song Z, Wu X. A simple anisotropic visco-hyperelastic constitutive model for cord-rubber composites. Compos Commun 2021;28:100957.
[31] Hamdi, et al. A fracture criterion of rubber-like materials under plane stress conditions. Polym Test 2006;25(8):994–1005.
[32] Charalambides, et al. Biaxial deformation of dough using the bubble inflation technique. I. Experimental. Rheol Acta 2002;41:532–40.
[33] Lev Y, Faye A, Volokh K. Experimental study of the effect of temperature on strength and extensibility of rubberlike materials. Exp Mech 2018;58:847–58.
[34] Volokh K. Mechanics of soft materials, vol. 337. Springer; 2019.
[35] Holzapfel GA. Nonlinear solid mechanics: a continuum approach for engineering science. Kluwer Academic Publishers Dordrecht; 2002.

[36] Volokh K. On irreversibility and dissipation in hyperelasticity with softening. J Appl Mech 2014;81(7):074501.
[37] Ogden RW. Large deformation isotropic elasticity–on the correlation of theory and experiment for incompressible rubberlike solids. Proc R Soc A 1972;326(1567):565–84.
[38] Ogden RW. Non-linear elastic deformations. Courier Corporation; 1997.
[39] MATLAB. MATLAB version: 9.13.0 (R2022b). Natick, Massachusetts, United States: The MathWorks Inc.; 2022, URL https://www.mathworks.com.
[40] ABAQUS. ABAQUS/Standard user's manual. United States: Dassault Systèmes Simulia Corp; 2021, URL https://www.3ds.com/products/simulia/abaqus.
[41] Gent A, Lindley P. Internal rupture of bonded rubber cylinders in tension. Proc R Soc A 1959;249(1257):195–205.
[42] Tangudom P, Thongsang S, Sombatsompop N. Cure and mechanical properties and abrasive wear behavior of natural rubber, styrene–butadiene rubber and their blends reinforced with silica hybrid fillers. Mater Des 2014;53:856–64.
[43] Ogden RW, Saccomandi G, Sgura I. Fitting hyperelastic models to experimental data. Comput Mech 2004;34:484–502.